International Journal of Thin Films Science and Technology

Microstructures and Optical Properties of Nanocrystalline Pr-doped BaTiO₃ Thin Film

Y. Iriani[*], *A. Suparmi, A. Marzuki and D. K. Sandi*

Physics Department, Faculty of Mathematics and Natural Sciences, Universitas Sebelas Maret, 57126, Indonesia

Abstract: This study aimed to synthesize Praseodymium (Pr) doped Barium Titanate (BT) or $Ba_{1-x}Pr_xTiO_3$ thin film and investigate the influence of Pr doping concentration on their microstructure and optical properties. The thin films with different Ba/Pr ratios (x=0, 0.03, 0.05, and 0.15) were fabricated on the quartz substrates using the sol-gel method with a spin coater. The microstructure and optical properties were observed by X-Ray Diffractometer (XRD) and UV-Vis Spectrophotometer, respectively. The microstructure results revealed that the lattice parameter, unit cell volume, and crystallite size of the Pr doped thin films decreased by the addition of Pr dopant. Meanwhile, the lattice strain and tetragonality were modified due to Pr doping. The optical measurement showed that the transmittance value advanced by giving Pr dopant, which caused the Pr-doped BT thin film to have higher refractive indices than the BT, thus making the Pr-doped samples possible to be anti-reflection coating. However, the bandgap is influenced by the thickness so that BT with the highest thickness possesses the highest bandgap, followed by Pr doping of 15%, 3%, and 5%.

Keywords: Praseodymium (Pr), Barium Titanate (BT), doping, thin film, microstructure, optical properties, bandgap, sol-gel method

1 Introduction

Recently, Barium Titanate (BaTiO₃), with the short name BT, has been one of the most attractive materials due to its remarkable features such as high dielectric constant, low optical losses, and low dielectric loss. Besides, BT also exhibits ferroelectric, piezoelectric, and pyroelectric with good non-linear optical properties [1,2,3,4]. Due to these properties, BT in bulk, as well as thin film form, has a wide range of applications, including flat panel displays [5], Ferroelectric Random Access Memory (FERAM), multilayer ceramic capacitors [6], pyroelectric detectors [4], sensors [7], switches [4], solar cell or photovoltaic [8], and other optoelectronic devices [4,6,9]. Moreover, BT possesses high optical transmittance and a high refractive index [2,4,6], so it is also employed as an effective window material and anti-reflection coating [2,4].

BT is a perovskite structure with ABO₃ formula with an oxygen octahedron structure, while Ba^{+2} cations and Ti^{+4} cations fill A-site and B-site, respectively [1]. The perovskite structure has a unique fundamental capability and high flexibility to host different ions, permitting various dopants to be introduced in BT lattices [1,5]. As known, doping with other elements is one of the principal technologies to enhance and alter the properties of materials [8]. Mainly, trivalent rare-earth (RE), especially lanthanide ions, are attractive dopants because they can perform as an acceptor and donor. They also can replace both A and B sites by considering the ionic radius of RE elements and the Ba/Ti ratio[3,5]. The RE dopants with large ionic radius tend to occupy the Ba^{2+}-site (A-site) such as Nd^{3+} (1.08Å) and La^{3+} (1.15Å). Meanwhile, the intermediate ones such as Er^{3+} (0.89Å) and Ho^{3+} (0.90Å) may replace both the A- and B-sites [4].

Many studies have reported the effects of RE lanthanide dopants, including La^{3+}, Yi^{3+}, Gd^{3+}, Nd^{3+}, Sm^{3+}, Er^{3+}, Mn^{3+}, Ho^{3+}, and Yb^{3+} in BaTiO₃ properties. It reveals that doping with these elements could enhance the microstructure, mechanical, electrical, dielectric, and optical properties of such materials by altering the crystal structure, grain size, morphology, phase transition, energy bandgap, and other characteristics related [1,2,3,4,10,11,12,13,14,15]. Further, Pr^{3+}which also includes the lanthanide ion, has been employed by researchers to improve the piezoelectric, optical properties, and photoluminescence behavior of ferroelectric compounds such as BaSrTiO₃, $(Ba_{1-x}Ca_x)$ TiO₃ ceramics, and BT ceramics [5,7,9,16,17]. Nonetheless, not as much effort has been made on Pr^{3+} doped BT thin film, even only on the development of the microstructure and the optical properties.

Therefore, this study aims to present a work of Pr^{3+} doped BT thin film synthesis with an analysis of the microstructure and optical properties as the influence of Pr^{3+} concentration.

[*]Corresponding author E-mail: yofent_iriani@staff.uns.ac.id

The fabrication employed the sol-gel method because of its advantages, such as easy operation, stoichiometry control, and low-cost equipment [12].

2 Experimental details

2.1. Preparation of Pr-doped BT

The thin films of Pr-doped BT with different molar ratios (x=0, x=0.05, x=0.10, and x=0.15) and the formula $Ba_{1-x}Pr_xTiO_3$ (BTPr) were made through the sol-gel method. The raw materials of Barium Acetate $[Ba(CH_3COO)_2]$, Praseodymium (III) Acetate Hydrate $[Pr(OOCH_3)_3.xH_2O]$, and Titanium (IV) Isopropoxide $[Ti(CH_3CH_3CHO)_4]$ were dissolved in the solvent agents of Acetic Acid $[CH_3COOH]$ and Ethylene Glycol by stirring using a magnetic stirrer. It then produced the solutions of BTPr. The thin films were prepared by depositing the solutions on quartz substrates via a Spin Coater. The rotation speed and deposition time were set at 300 rpm for 30 s, followed by pyrolysis on a hot plate at a temperature of 150ºC. The deposited films were then annealed for 2 h at a temperature of 950ºC. The samples would be named as BT, BTPr3, BTPr5, and BTPr15 for various Pr concentration-doped BT of x=0, x=3%, x=5%, and x=15%, respectively.

2.2. Characterization of Pr-doped BT thin film

The samples were tested using Philips PW 3710/40 kV X-ray Diffraction (XRD) with Cu Kα radiation (λ = 1.5406 Å) for the crystal properties analysis. Scanning Electron Microscopy (SEM) was performed on the samples for morphological feature analysis and to estimate the thickness. Meanwhile, the UV-VIS Spectrophotometer was employed in a wavelength range of 200-800 nm for the optical properties' investigation.

3 Results and Discussion

Figure 1 presents the XRD profiles of BT and Pr-doped BT deposited on the quartz substrate with various concentration ratios. The profiles agree with ICDD database number #831800, which reveals a single-phase polycrystalline barium titanate with a tetragonal structure (*P4mm* space group). However, there are impurities detected marked with (*). As perceived from the magnification of the (101) peak, it exhibits that the main peak from BT to BTPr15 shifts toward a smaller d-spacing. It means that the shift convoys the change in the lattice constant of the samples. This indicates that the Pr dopant has entered the crystal structure and replaced the Ba-site. The Pr^{+2} ionic radius is 0.99 Å while Ba^{+2} is 1.35 Å. Based on Bragg's Law as Eq.1, the θ diffraction angle is inversely proportional to d-spacing. In contrast, d-spacing is proportional to the lattice number, and thus if the lattice constant becomes smaller due to doping, it causes the d-spacing to be smaller, which moves it to the left.
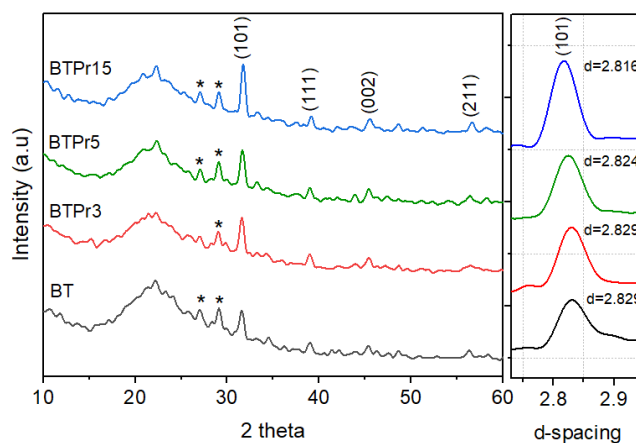
Fig. 1: (left) XRD profiles of BT and BTPr thin films, (right) the magnification of (101) peak as a function of d-spacing

Table 1: The crystal structure of BT and BTPr thin films

Samples	BT	BTPr3	BTPr5	BTPr15
Concentration $(Ba_{1-x}Pr_xTiO_3)$	x=0	x=0.03	x=0.05	x=0.15
Lattice Constant (Å)				
$a = b$	3.9986	3.9956	3.9958	3.9862
c	3.9972	3.9922	3.9901	4.0187
Cell Volume ($Å^3$)	63.91	63.735	63.709	63.857
d-spacing(d_{101})	2.829	2.829	2.824	2.816
Crystallite Size (nm)	44	41	24	27
Lattice Strain	0.0109	0.0333	0.0096	0.0098

The crystal structure of the BT and BTPr thin films is shown in Table 1, calculated from the XRD data. The lattice constant in this study was computed by lattice geometry for tetragonal structure as Eq. 2. In which *d* is interplanar space, h k l is crystal plane orientation, a b c is lattice constant, and *θ* is diffraction angle. It is observed that the lattice constant, unit cell volume, and thus d-spacing of all Pr-doped BT films are reduced as a result of doping as compared to the undoped BT film. As mentioned, the lattice reduction is led by the substitution of Ba^{2+} by Pr^{3+} dopant. Even so, the decrease in the lattice constant, unit cell volume, and so the d-spacing of the BTPr3 and BTPr5 films are proportional to the more Pr concentration. However, the lattice constant and unit cell volume of BTPr15 increases instead of the BTPr3 and BTPr5 films, though it is still slightly smaller than BT's values. As reported, this condition could be considered because of the defect formation within the lattice constant due to doping.[13] Vacancies might be generated when +3 state cation (Pr^{3+}) substitutes +2 state cation (Ba^{2+}), thus inhibiting the space within the lattice and allowing the lattice constant to increase.

$$\frac{\lambda}{2d} = \sin\theta \qquad (1)$$

$$\frac{1}{d^2} = \frac{h^2+k^2}{a^2+b^2} + \frac{l^2}{c^2} \quad (2)$$

$$D = \frac{0.9\,\lambda}{\beta \cos\theta} \qquad (3)$$

$$\beta \cos\theta = \frac{0.9\,\lambda}{D} + 4\varepsilon \sin\theta \quad (4)$$

The crystallite size was estimated via the Scherer equation as Eq. 3. D is crystallite size, λ is the wavelength of the X-ray source, and β is Full-Width Half Maximum (FWHM). Overall, with the addition of Pr content, the crystallite size of the Pr-doped BT is smaller than BT. The decrement in crystallite size might be attributed to the decrease in the lattice constant and cell volume of the samples due to Pr^{3+} doping. Besides, this trend of the crystallite size values is appropriate with the lattice and cell volume values trend of the respective sample with the crystallite size seems to increase lightly from 24 nm for BTPr3 to 27 nm for BTPr15. The crystallite size values demonstrate that all samples are nanocrystalline.

Meanwhile, the lattice strain (ε) was determined through the William-Hall way using Eq. 4 [18]. By plotting $4\sin\theta$ (x-axis) and $\beta \cos\theta$ (y-axis), the lattice strain can be determined from the slope of the plot. It exhibits that the Pr dopant changes the lattice strain of the samples. The BTPr3 possesses the largest strain of 0.0333, followed by BT, BTPr15, and BTPr3, which are 0.0109, 0.0096, and 0.0098, respectively.

Figure 2 displays the SEM images of the surface of BT, BTPr3, BTPr5, and BTPr15 films. From the figure, the grains of the undoped BT film are fine with a smooth micro-crack. Even so, the surface appears very dense than those of the Pr-doped BT. For the doped ones, the grains are larger and experience more agglomeration with more Pr. Additionally, more porous is observed on the films with higher Pr concentration, while the crack only appears on the BT surface.

Figure 3a shows the UV-Vis transmittance spectra of the BT and BTPr thin films. Both the BT and BTPr films are transparent in the visible light region. The absorption edge is around the wavelength range of 325-370 nm. As the change in the Pr number, there is no significant shift in the absorption edge. However, doping affects the transmittance values of the films at the wavelength range of 400-800 nm. As perceived, all Pr-doped BT samples have higher transparency than the undoped BT. The BTPr15 has the highest transparency, about 80%, followed by BTPr3 and BTPr5, which have a slight difference in the value of about 75%. The transmittance might be associated with crystallite size. The crystallite size enlargement may impact the grain boundaries and bring more compact crystal layers.

Further, it has been stated that more dopants may cause vacancy because of the substitution of Pr^{3+} in the Ba^{2+} site, which means the crystal layers are not as compact as the undoped ones. Hence, the film with bigger crystallite, in this case, BT with the size of 439 nm, has the lowest transmittance. Meanwhile, BTPr15 with vacancies available possesses the highest transmittance.
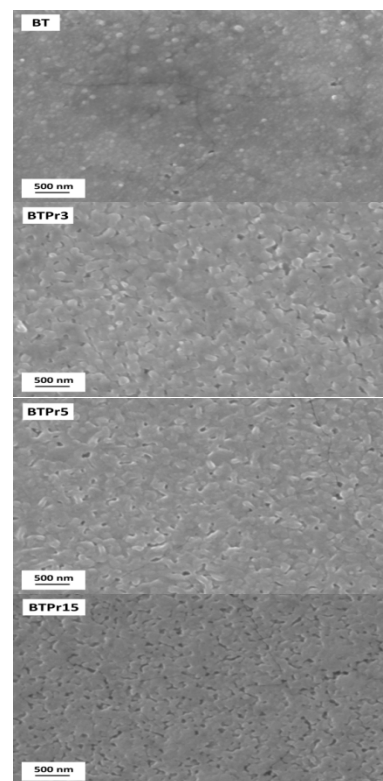
Fig. 2: Morphological features of BT and BTPr thin films
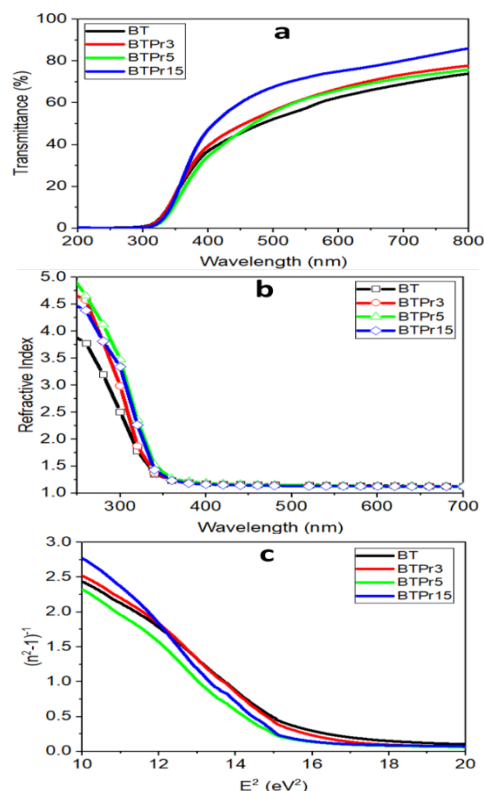
Fig. 3: (a) Transmittance spectra and (b) refractive indices of the BT and BTPr thin films as a function of wavelength, and (c) the relationship between $(n^2-1)^2$ and E^2 of the BT and BTPr thin films

Through the transmission data and the Swanepoel method [19], the refractive index as a function of the wavelength of all samples can be plotted in Figure 3b. It can be seen that the Pr doping leads to the advance in the refractive index of the film. The values are about 3.7 and 4.7 at 250 nm, decreasing as the higher wavelength then becomes constant at the wavelength above 400 nm. The alteration between the refractive indices of the samples is an indication of the structural modifications that occurred due to doping during the fabrication process. The high refractive index makes Pr-doped BT possible for anti-reflection coating. Further, Figure 3c presents the relationship between $(n^2-1)^2$ and E^2, denoting the dispersion energy of the materials. Here, BTPr15 shows the highest dispersion energy compared to the others, while the curves between BT and BTPr3 coincide.

Table 2: Thickness and bandgap values of BT and BTPr films

Samples	BT	BTPr3	BTPr5	BTPr15
Thickness (nm)	155	77	55	117
Band-gap (eV)	3.64	3.51	3.32	3.60

Table 2 lists the thickness of BT and BTPr films which is significantly different at each doping number. However, here, we didn't observe the doping effects on the films' thickness. Indeed, we used it to calculate the bandgap value of the films via the Tauc's Plot relation (Eqs.). In which A, α, h, v and E_g are a constant, absorption coefficient, Planck constant, frequency (hv is the photon energy) and the optical band gap, respectively. E_g could be obtained by making the plot of $(\alpha hv)^2$ vs. hv and extrapolating the linear part of the abscissa ($(\alpha hv)^2 = 0$) as shown in Figure 4.

$$(\alpha hv)^2 = A(hv - E_g) \quad (5)$$
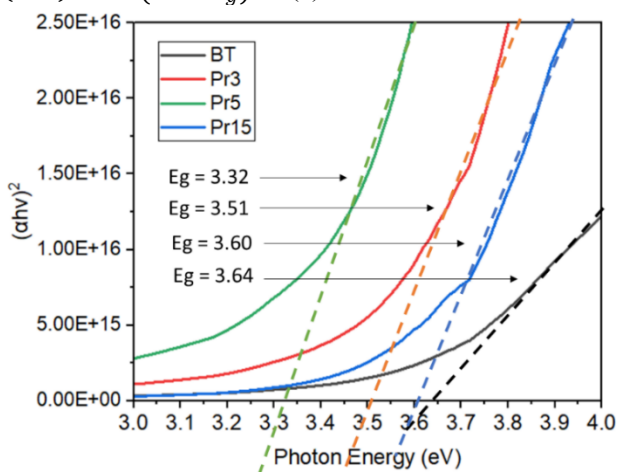
Fig. 4: The plot of $(\alpha hv)^2$ vs hv and line extrapolation to $(\alpha hv)^2 = 0$ of the BT and BTPr films

As seen in Figure 4, the bandgap of the BT is 3.64 eV and decreases as the Pr doping. Nevertheless, the decrement is not linear with the Pr number because BTPr3, BTPr5, and

BTPr15 bandgap values are 3.51, 3.32, and 3.60 eV, respectively. The bandgap value can be associated with the crystallite size of the material. In non-thin film materials, the morphology and thickness do not influence the bandgap. However, in the thin film, there is a quantum effect applied so that the thickness can affect the bandgap energy. In this study, we could not discuss the effects of the crystal property and surface morphology on the bandgap because the data are not in line with it. Indeed, since the significant distinction of the film's thickness and the trend of bandgap values are in line with the thickness, we consider that the bandgap values are affected by the thickness. Figure 4 and Table 1 show that the films with lower thickness results in lower bandgap energy values and vice versa.

4 Conclusions

The influence of Pr doping concentration on BT thin film's microstructure and optical properties has been observed by XRD, SEM, and UV-Vis Spectrophotometer, respectively. The results exposed that the lattice parameter, unit cell volume, and crystallite size of the Pr doped thin films shrink with the addition of Pr dopant. On the other hand, the crystallite size enlarges while the lattice strain and the tetragonality modify because of the Pr doping. The optical measurement displays that the transmittance value advanced by giving Pr dopant, which leads the Pr-doped BT thin film to possess higher refractive indices than the BT. However, the bandgap is influenced by the thickness so that BT with the highest thickness possesses the highest bandgap, followed by BTPr15, BTPr3, and BTPr5.

Acknowledgements

References

[1] A. Alshoaibi, M. B. Kanoun, B. Ul-Haq, S. Al-Faify and S. Goumri-Said, Insights into the Impact of Yttrium Doping at the Ba and Ti Sites of BaTiO₃ on the Electronic Structures and Optical Properties: A First-Principles Study, *ACS Omega*, **5**, 15502 (2020).

[2] A.Y. Fasasi, B. D. Ngom, J. B. Kana, R. Bucher, M. Maaza, C. Theron and U. Buttner, Synthesis and characterization of Gd-doped BaTiO₃ thin films prepared by laser ablation for optoelectronic applications, *J. Phys. Chem. Solids*, **70**, 1322 (2009).

[3] M. A. Gomes, A. S. Lima, K. I. B. Eguiluz and G. R. Salazar-Banda, Wet chemical synthesis of rare earth-doped barium titanate nanoparticles, *J. Mater. Sci.*, **51**, 4709 (2016).

[4] M. K. Mahata, T. Koppe, K. Kumar, H. Hofsass and

U. Vetter, Upconversion photoluminescence of Ho^{3+}-Yb^{3+} doped barium titanate nanocrystallites: Optical tools for structural phase detection and temperature probing, *Sci. Rep.*, **10**, 8775 (2020).

[5] J. Li, Y. J. Wu and M. Kuwabara, Enhancement of Luminescent Properties of Sol-Gel-Derived $BaTiO_3$: Pr, *Key Eng. Mater.*, **301**, 197-200 (2006).

[6] A. Karvounis, F. Timpu, V. V. Vogler-Neuling, R. Savo and R. Grange, Barium Titanate Nanostructures and Thin Films for Photonics, *Adv. Opt. Mater.*, **8**, 2001249 (2020).

[7] T. Wei, N. Haiyong, Z. Qiuhong and D. Jianhong, Novel optical temperature sensor based on emission in Pr^{3+} doped ferroelectric $Ba_{0.7}Sr_{0.3}TiO_3$, *RSC Adv.*, **8**(42), 23996 (2018).

[8] X. Luo, Y. Li, K. Liu and J. Zhang, Electron transport enhancement of perovskite solar cell due to spontaneous polarization of Li^+-doped $BaTiO_3$, *Solid State Sci.*, **108**, 106387 (2020).

[9] A. W. Miroslaw, M. Bu'cko, J. Lis, A. Toczek and L. Kozielski, Photoluminescence and electrical properties in Pr-modified $(Ba_{1-x}Ca_x)TiO_3$ multifunctional ceramics, *Process. Appl. Ceram.*, **14**, 77-82 (2020).

[10] D. K. Sandi, Y. Iriani and D. Fasquelle, Microstructure and Optical Properties of Zirconium Co-Doped Barium Titanate Thin Films on Quartz Substrates, *Key Eng. Mater.*, **907**, 44-49 (2021).

[11] Y Iriani, D. K. Sandi, F. Nurosyid, H. Widiyandari and R. Suryana, Structural and Optical Studies of Lithium Doped Barium Titanate, *Key Eng. Mater.*, **904**, 358-362 (2021).

[12] Y. C. Teh, A. A. Saif and P. Poopalan, Sol-Gel Synthesis and Characterization of $Ba_{1-x}Gd_xTiO_{3+\delta}$ Thin Films on SiO_2/Si Substrates Using Spin-Coating Technique, *Mater. Sci. (MEDŽIAGOTYRA)*, **23**, 51-56 (2017).

[13] A. Kumari, K. Kumari, F. Ahmed, A. Alshoaibi, P. A. Alvi, S. Dalela, M. M. Ahmad, R. N. Aljawfi, P. Dua, A. Vij and S. Kumar, Influence of Sm doping on structural, ferroelectric, electrical, optical and magnetic properties of $BaTiO_3$, *Vacuum*, **184**, 109872 (2021).

[14] A. Meneses-Franco, M. Campos-Vallette, S. O. Vasquez and E. A. Soto-Bustamante, Er-Doped Nanostructured $BaTiO_3$ for NIR to Visible Upconversion, *Materials (Basel)*, **11**, 1950 (2018).

[15] A. Semenov, A. Dedyk, I. Mylnikov, O. Pakhomov, A. Es'kov, A. Anokhin, V Krylov, A. Burovikhin, Y. Pavlova, A. Tselev and A. Kholkin, Mn-Doped $BaTiO_3$ Ceramics: Thermal and Electrical Properties for Multicaloric Applications, *Materials (Basel)*, **12**, 3592 (2019).

[16] M. K. Adak and D. Dhak, Assessment of strong relaxation on $BaTiO_3$ modified by Mn^{2+} and Pr^{3+}, K^+ at A- and B− site respectively, *Mater. Res. Express*, **6**, 125082 (2019).

[17] H. Zou, D. Peng, G. Wu, X. Wang, D. Bao, J. Li, Y. Li, and X. Yao, Polarization-induced enhancement of photoluminescence in Pr^{3+} doped ferroelectric diphase $BaTiO_3$-$CaTiO_3$ ceramics, *J. Appl. Phys.*, **114**, 073103 (2013).

[18] V. D. Mote, Williamson-Hall analysis in estimation of lattice strain in nanometer-sized ZnO particles, *J. Theor. Appl. Phys.*, **6**, 1-8 (2012).

[19] R. Swanepoel, Determination of the thickness and optical constants of amorphous silicon, *J. Phys. E: Sci. Instrum.*, **16**, 1214 (1983).